



OPEN

Tuning of silicon nitride micro-cavities by controlled nanolayer deposition

Dmitry A. Kalashnikov^{1✉}, Gandhi Alagappan², Ting Hu³, Nelson Lim¹, Victor Leong¹, Ching Eng Png² & Leonid A. Krivitsky¹

Integration of single-photon emitters (SPEs) with resonant photonic structures is a promising approach for realizing compact and efficient single-photon sources for quantum communications, computing, and sensing. Efficient interaction between the SPE and the photonic cavity requires that the cavity's resonance matches the SPE's emission line. Here we demonstrate a new method for tuning silicon nitride (Si_3N_4) microring cavities via controlled deposition of the cladding layers. Guided by numerical simulations, we deposit silicon dioxide (SiO_2) nanolayers onto Si_3N_4 ridge structures in steps of 50 nm. We show tuning of the cavity resonance exceeding a free spectral range (FSR) of 3.5 nm without degradation of the quality-factor (Q-factor) of the cavity. We then complement this method with localized laser heating for fine-tuning of the cavity. Finally, we verify that the cladding deposition does not alter the position and spectral properties of nanoparticles placed on the cavity, which suggests that our method can be useful for integrating SPEs with photonic structures.

Integrated quantum photonic devices are critical elements for future quantum networks, quantum computers, and sensors^{1–8}. One of the essential elements of such a device is a single-photon emitter (SPE), which is coupled to a high Q-factor cavity. Upon excitation of the SPE, the single photon is emitted in the cavity mode and then routed to an optical network for manipulation and detection^{9–12}. Such an interface requires a nearly perfect matching of the emission line of the SPE with the resonance line of the cavity. Given the intrinsic uncertainty in the SPE emission line and the cavity's resonances, their matching requires active tuning of the SPE and/or the cavity. While tuning the emission wavelengths of the SPE is possible, for example, by applying electric fields^{13–15}, it is arguably more practical to tune the resonance line of the photonic cavity.

Methods of tuning micro-cavities include thermal and electro-optical tuning, application of mechanical stress, and post-fabrication trimming with functionalization of the surface or patterning of the cladding material^{16–27}. Most of these methods allow accurate tuning of the cavity resonances with real-time control. However, they are not free from technical challenges. For example, thermal and electrical tuning require a significant amount of electrical power to be delivered into the chip, especially when broadband tuning across a full free spectral range (FSR) is required^{18–20,23–26}. Moreover, in this case, the electrical contacts should be positioned next to the cavities, which complicates the fabrication process and might degrade the cavity performance¹⁸. Methods based on the deposition of a photochromic film or the functionalization with a laser addressable polyelectrolyte strongly depend on the thickness of the applied material, which is hard to control. These methods may also degrade the optical properties of the cavities due to surface modification^{16,17}. Post-fabrication trimming of a cladding material requires precise patterning with electron beam lithography, and the cladding itself prevents efficient coupling to integrated SPEs²⁷. Stress-based approaches require sophisticated fabrication and a large device size to tune across the full FSR^{21,22}.

Silicon nitride (Si_3N_4 , or SiN) stands out as a material of choice for many device prototypes due to its CMOS compatibility, broad transparency range, and relatively high refractive index ($n \sim 2$)^{28–31}. However, the thermo-optic coefficient of Si_3N_4 is approximately one order of magnitude lower than for silicon³², which makes it challenging to implement thermal-based tuning strategies described above. Moreover, at cryogenic temperatures required to optimally operate many SPEs, the Si_3N_4 thermo-optic coefficient becomes even smaller.

¹Institute of Materials Research and Engineering, Agency for Science, Technology, and Research (A*STAR), 2 Fusionopolis Way, #08-03 Innovis, Singapore 138634, Singapore. ²Institute of High Performance Computing, Agency for Science, Technology, and Research (A*STAR), Fusionopolis, 1 Fusionopolis Way, #16-16 Connexis, Singapore 138632, Singapore. ³Institute of Microelectronics, Agency for Science, Technology, and Research (A*STAR), 2 Fusionopolis Way, #08-02 Innovis, Singapore 138634, Singapore. ✉email: Dmitry_Kalashnikov@imre.a-star.edu.sg

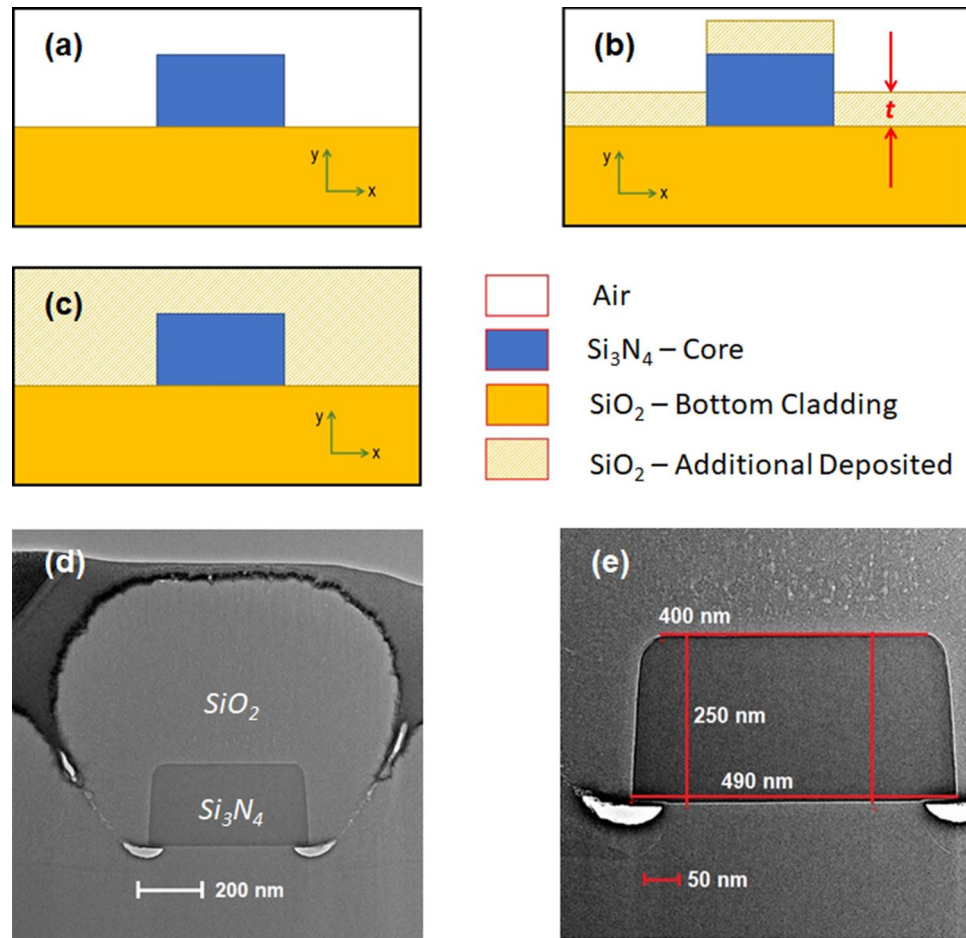


Figure 1. Distribution of SiO₂ cladding around the Si₃N₄ waveguide. (a) Schematic of a ridge waveguide with lower and upper cladding being air and SiO₂, respectively. (b) Schematic for theoretical consideration with an additional layer of SiO₂ deposited. (c) A channel waveguide, with the upper and lower cladding being SiO₂. (d) TEM cross-section of a $w=480$ nm Si₃N₄ waveguide after depositing a $t=500$ nm thick SiO₂ cladding. (e) Measured dimensions of a $w=480$ nm Si₃N₄ waveguide.

In this work, we propose and realize a method for broadband tuning of Si₃N₄ cavities. It is based on depositing a silicon dioxide (SiO₂) cladding of controlled thickness over Si₃N₄ cavities with tens of nanometers step size. We show that within the range of thicknesses of the cladding layer from 200 to 500 nm, we can tune the resonance position within one FSR of 3.5 nm. Although this method can only tune the resonance in relatively coarse steps, it can be complemented with other methods for fine tuning. Nevertheless, this method allows us to first bring the cavity resonances and SPE emission wavelength closer to a rough approximation, before fine-tuning with another approach. To this end, we demonstrate fine tuning of the cavity by applying laser heat after depositing the SiO₂ cladding. We also show that SiO₂ deposition does not change the position and spectral properties of the SPEs (a diamond nanocrystal in our case) that were earlier placed on the ring cavity.

Theoretical model

We consider a ridge waveguide with the lower and upper cladding being SiO₂ and air, respectively. Figure 1a shows the cross-section of the ridge waveguide. The Si₃N₄ core has a refractive index of 2.087 (measured value at 737 nm) with width w , and height $h=250$ nm. In this work, we consider two nominal design widths, $w=330$ and 480 nm. The geometrical parameters of the waveguides are designed to support single-mode propagation for both TM and TE polarizations of light with low losses.

We assume that the deposition of SiO₂ forms a layer with thickness t on top of the lower cladding layer and core layer, parallel to the x -axis. This is schematically shown in Fig. 1b. The normal line of the additional layer is parallel to y -axis. In reality, there will be a thin layer of SiO₂ (with the normal line along the x -axis) surrounding the vertical edges of the core. However, a deterministic value for the thickness of such a layer is hard to obtain. Hence, it has been neglected in the theoretical model. The ridge waveguide (before deposition) represents $t=0$, and another extreme $t=\infty$ represents a channel waveguide (Fig. 1c). The example of real distribution of SiO₂ over Si₃N₄ waveguide is shown in Fig. 1d,e, (see “Device fabrication” section).

The waveguide optical properties as a function of t are obtained by solving the two-dimensional time-independent Maxwell’s equation³³. In Fig. 2, we exhibit the optical mode profile of the waveguides ($w=480$ nm)

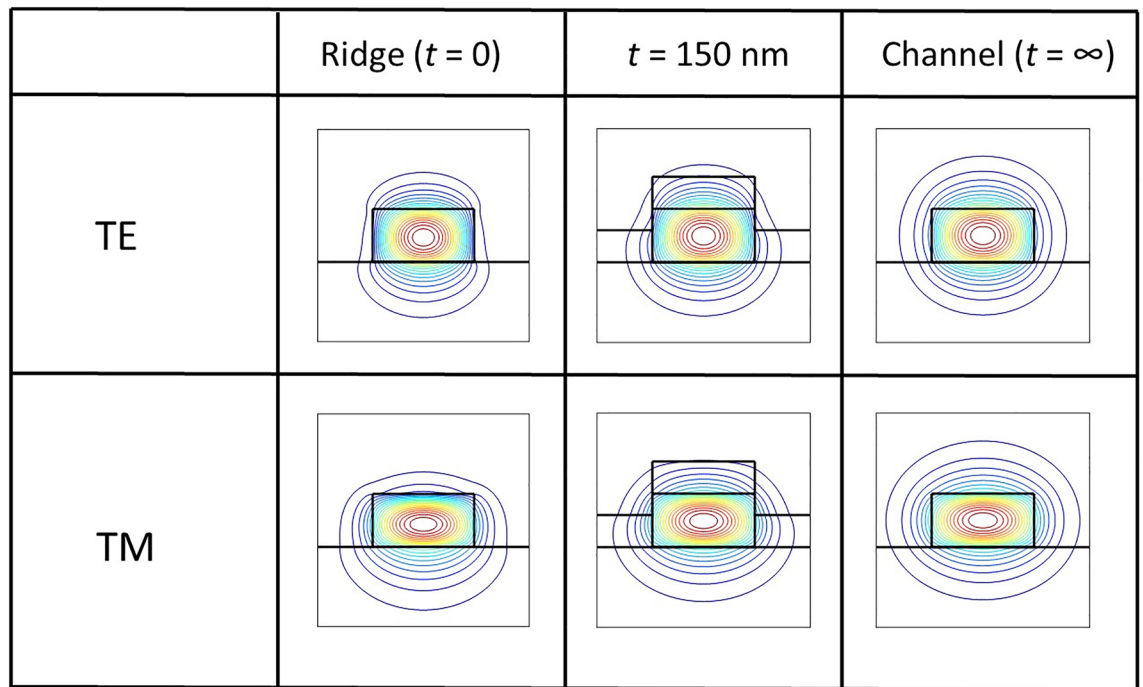


Figure 2. Simulation results for the contour plots of the optical mode (H -field) for the waveguide with $h = 250$ nm, $w = 480$ nm. The red (blue) color represents the maxima (minima).

for $t = 0$ (ridge), $t = 150$ nm, and $t = \infty$, for both TE and TM polarizations. For TE polarization, the E_x and H_y components are dominant. On the other hand, for TM polarization, E_y and H_x are dominant. The contrast in refractive index between the upper cladding (air) and the core is larger than the contrast between the lower cladding (SiO_2) and the core of the ridge waveguide. Therefore, the vertical symmetry is broken in the optical mode pattern. Moreover, the degree of mode penetration is higher in the lower cladding than in the upper cladding. As t increases, the upper cladding is modified, and the effective contrast in the refractive index is reduced. Consequently, the asymmetry decreases, and the degree of mode penetration in the upper cladding region increases. In the extreme case of $t = \infty$ (channel waveguide), the symmetry is restored.

The effective refractive index is linked to the group refractive index $n_g(t)$ by the following equation,

$$n_{\text{eff}}(\lambda, t) = n_g(t) + \lambda F(t) \quad (1)$$

where $F(t) = dn_{\text{eff}}(t)/d\lambda$.

If a microring cavity is constructed using a waveguide of effective refractive index $n_{\text{eff}}(\lambda, t)$, then the resonance frequency can be obtained from the resonance condition $m\lambda_{\text{res}} = n_{\text{eff}}(\lambda, t)L$, where $L = 2\pi R$ is the round-trip length, and m is a positive integer³⁴. Using this condition, it is straightforward to express $\lambda_{\text{res}}(t)$ using Eq. (1) as

$$\lambda_{\text{res}}(t) = \frac{\frac{L}{m}n_g(t)}{1 - \frac{L}{m}F(t)} \quad (2)$$

Figure 3a,b show $\lambda_{\text{res}}(t)$ calculated for values of m that most closely match the experimental data (see the experimental section below). From these figures we can see that the changes in $\lambda_{\text{res}}(t)$ are large and small for small and large t , respectively. Therefore, a logistic curve would give a best and representative estimate for the evolution of $\lambda_{\text{res}}(t)$. The fitting to a logistic curve can be easily done using a single layer neural network with a sigmoid transfer function, and trained it with data points generated by Eq. (2). The neural network model is employed for a better generalization, and to avoid overfitting³⁵. With this formalism, for the range of t considered here, we find that $\lambda_{\text{res}}(t)$ can be well approximated by the relationship

$$\lambda_{\text{res}}(t) = \lambda_{\infty} - \frac{B}{1 + e^{at}} \quad (3)$$

where B and a are positive constant coefficients. The fitted values of B and a are tabulated in Table 1. For large t , $\lambda_{\text{res}}(t) = \lambda_{\infty}$; for small t , using Taylor expansion we have $\lambda_{\text{res}}(t) = \lambda_{\infty} - \frac{B}{2} + \frac{aB}{4}t + \dots$. Clearly, the cavity resonance wavelength varies linearly for small t , and eventually saturates as t increases. This asymptotic behaviour is true for any mode order m .

	TE		TM	
	B	a	B	a
$w = 330$ nm				
Expt.	0.20	18.03	0.13	17.72
Theory (mode 1)	0.10	14.08	0.05	10.60
Theory (mode 2)	0.10	14.15	0.05	10.64
$w = 480$ nm				
Expt.	0.04	16.22	0.05	18.03
Theory (mode 1)	0.04	14.49	0.03	11.41
Theory (mode 2)	0.04	14.55	0.03	11.45

Table 1. The values of B and a in Eq. (3), obtained from fits to experimental data and theoretical models presented at Fig. 3a,b. Mode 1 has a higher value of m than mode 2.

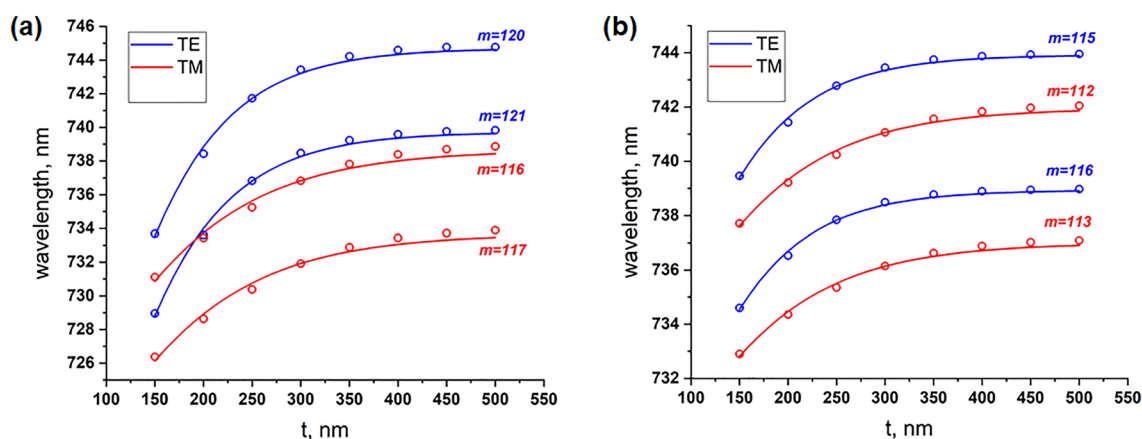


Figure 3. Theoretically estimated resonance wavelengths of the ring cavity (radius $R = 8 \mu\text{m}$) for waveguide widths (a) $w = 330$ and (b) $w = 480$ nm, respectively. Circles are obtained from Eq. (2), while the solid lines are fits given by Eq. (3).

Materials and experimental techniques

Device fabrication. We fabricated Si_3N_4 micro-cavity devices consisting of ring cavities (radius $R = 8 \mu\text{m}$) coupled to straight bus waveguides with the same height $h = 250$ nm and width $w = 330$ nm or 480 nm. The gap between the bus and the ring is 160 nm, which is close to the critical gap of the ring cavity that maximizes the bus-cavity coupling. For the efficient coupling of light from a lensed optical fiber, each waveguide has tapered edge couplers (minimum width 150 nm) for the efficient transformation of the TEM_{00} mode of the lensed fiber to propagating modes of the Si_3N_4 waveguide.

The fabrication started at a commercial CMOS foundry with a standard 8-in. silicon wafer. A $3.1 \mu\text{m}$ -thick SiO_2 layer and a 250 nm-thick Si_3N_4 were formed using the thermal oxidation and low-pressure chemical vapor deposition (LPCVD) method. Before deposition of the Si_3N_4 layer, chemico-mechanical polishing (CMP) was used to reduce the thickness of the SiO_2 to $3 \mu\text{m}$. Then 248 nm KrF deep ultraviolet (DUV) lithography and inductively coupled plasma (ICP) etch were used to define the Si_3N_4 waveguides and ring resonators. This was followed by the upper cladding deposition of $3.4 \mu\text{m}$ -thick SiO_2 via plasma-enhanced chemical vapor deposition (PECVD). To expose the Si_3N_4 ring resonators to the air, a window was opened in the upper cladding layer of SiO_2 using lithography and a combination of dry etch ($3.1 \mu\text{m}$) and wet etch ($0.3 \mu\text{m}$). The edge coupler for light coupling with fiber was fabricated by the deep etch of the cladding and Si substrate to realize a trench.

The layers of SiO_2 cladding were deposited in steps of 50 ± 5 nm by ICP-CVD Oxford PlasmaPro System 100 in SiH_4 and N_2O atmosphere at 4 mTorr pressure, 150°C temperature, and 1000 W ICP power. To ensure the thickness accuracy of the cladding layers, each deposition was preceded by calibration measurements, where SiO_2 was deposited on a blank target and studied under an ellipsometer (J.A. Woollam V-VASE). After each deposition, we measured the cavity resonance wavelengths in our experimental setup. The accuracy of SiO_2 deposition, its distribution around the waveguide and the cavity were studied via cross-section transmission electron microscope (TEM) images (Fig. 1d,e).

High-pressure high-temperature (HPHT) nanodiamonds containing silicon-vacancy (SiV) centers³⁶ were suspended in isopropanol (0.1 wt%), ultrasonicated for 30 min, then randomly deposited on the device by spin-coating at 2000 rpm for 5 min. Under scanning electron microscope (SEM) imaging, we find that approximately 30% of the Si_3N_4 cavities had nanodiamonds deposited directly on top of them.

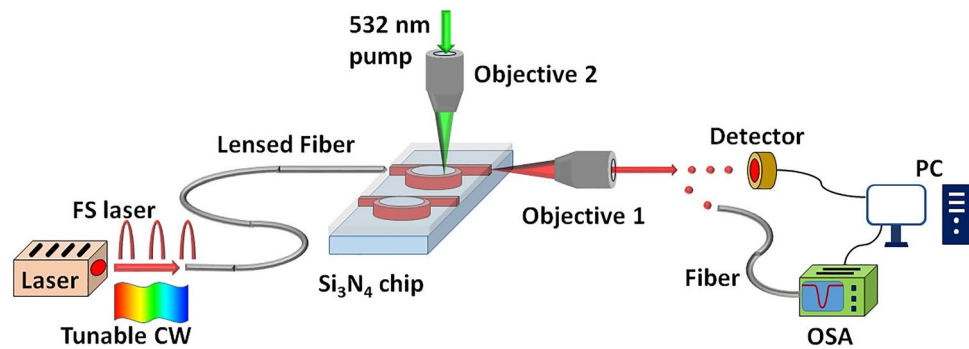


Figure 4. Sketch of the experimental setup: light from broadband fs laser or tunable CW laser is coupled to the lensed fiber. Lensed fiber injects the light into the Si_3N_4 micro-cavity device. At the output of the device the transmitted light is collected and collimated with $50\times$ objective (Objective 1). Then the light is sent either to the photodetector (for tunable CW laser) or to the optical spectral analyzer (OSA) via a single-mode fiber (for fs laser). The 532 nm pump laser is focused onto the micro-cavity device by $100\times$ objective (Objective 2) for confocal and heating measurements.

Measurements. We performed measurements at wavelengths of around 737 nm by probing the chip with laser light. It was coupled to the waveguide by a lensed fiber (Oz Optics), and the transmitted light was collected with a $50\times$ objective lens (Olympus) at an opposite edge of the chip, see Fig. 4. We first used attenuated broadband femtosecond (80 fs) laser pulses (Mai Tai, SpectraPhysics) as the input, coupled the transmitted signal to a single-mode fiber, and sent it to an optical spectral analyzer (OSA, Yokogawa AQ6370) with a spectral resolution of 37 pm in the visible range. With its spectral width of over 10 nm, the fs-pulses covered several resonances and allowed a fast estimation of the resonance position. The precise measurement of resonances is then performed by a narrowband (linewidth < 1 MHz) tunable continuous-wave (CW) diode laser (Sacher). We sweep the laser wavelength in the vicinity of the resonance and measure the light intensity passing through the cavity using an optical power meter (Thorlabs) placed after the objective lens. The wavelength of the tunable laser was measured by a wavelength meter (HighFinesse, Model WS-7) with an accuracy of 60 MHz and resolution of 2 MHz. This allowed us to measure the quality factor and fine shifts of the resonance. The devices were placed on a metallic mount which served as an effective heat sink. The ambient temperature fluctuation range was within 0.5°C over the course of the measurements, within which we did not observe any shift of resonant lines. The experimental data was acquired and post-processed at the PC using self-written software in Python.

A scanning confocal microscope integrated into the test setup was used to measure the fine resonance shift under the laser heating, as well as the spectra of SiV centers in the nanodiamonds before and after SiO_2 deposition. The 532 nm pump laser was scanned using a fast steering mirror (Newport FSM-300) and projected with a 4f lens system to a $100\times$ objective (NA = 0.9, Nikon), which focused the beam onto the chip. The focused spot size was measured to be 500 nm with a knife blade mounted on a piezo stage (Thorlabs NanoMax Max311). The emission was collected by the same $100\times$ objective, and coupled to a single mode fiber (SMF). The signal from SMF was sent either to an avalanche photodetector (PerkinElmer SPCM-AQRH-14FC) to obtain the confocal scan map, or to a spectrometer equipped with an EMCCD camera (Princeton Instruments, 1200 Grooves/mm).

To apply laser heating experiment, the confocal scan map was used to direct the focused 532 nm laser onto the cavity. The tunable CW laser was swept to measure the shift of the cavity resonance. The position of the beam spot was optimised by moving it across the ring cavity in steps of 400 nm to get the largest resonant line shift.

For the measurements of SiV spectra, the confocal scan map was used to locate nanodiamonds containing SiV on the cavities. Using a 532 nm pump power of 0.4 mW, the SiV photoluminescence was collected via the confocal microscope and sent to the spectrometer, where the collected signal was automatically digitized by the included software (LightField).

Results and discussions

Demonstration of tuning using SiO_2 deposition. For very thin layers deposited onto the cavity, we cannot precisely characterize the resonance shift, as it is larger than one $\text{FSR} = \lambda^2 / (2\pi n_{\text{eff}} R)$. The measured Q-factor is on the order of 10^4 , which we confirm to be unaffected by the deposition of the cladding layers, see Supplementary Fig. S1. Starting from some finite thickness of SiO_2 layer (200 nm in our case), the resonance shift stays within one FSR, and we can track it within the same order (m in Eq. 2). Figure 5 shows the experimentally measured shifts of resonance wavelengths and their theoretical fits as a function of t . The theoretical curves are obtained by averaging the numerical derivatives of the respective numerical fits of the two modes in Fig. 3a,b (see Table 1 for the parameters of the fits). We obtain a generally good agreement between the theoretical predictions and experimental measurements; the observed discrepancies are due to uncertainties in material properties as well as some constraints of the theoretical model. For example, it does not include a thin SiO_2 layer deposited around the vertical edges of the core (with the normal of the layer parallel to x -axis, see Fig. 1). Therefore, a good numerical agreement can be obtained by considering the amount of tuning after every increment in the thickness.

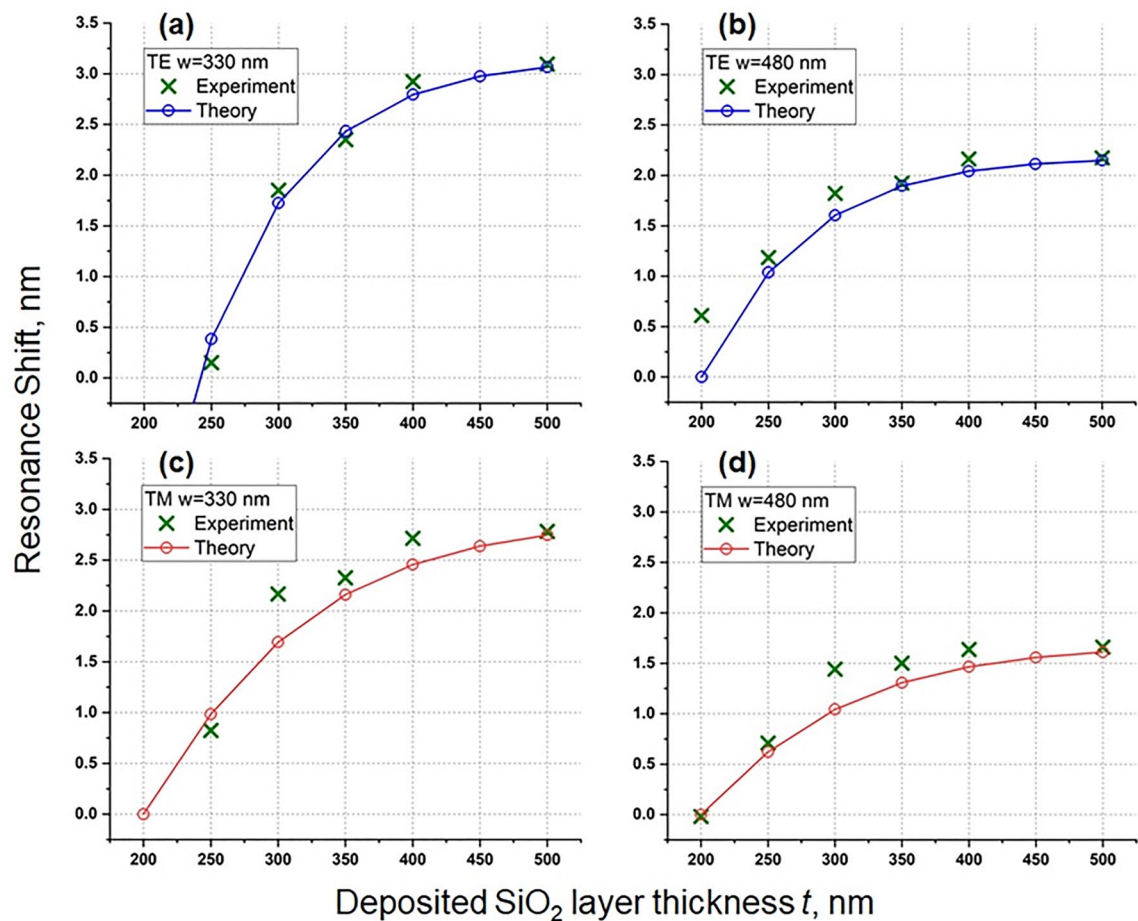


Figure 5. Experimental results for tuning the resonance wavelength as a function of additional SiO₂ layer thickness. The experimental points are plotted as green crosses, while solid lines represent theoretical curves. Red and blue colors represent TM and TE polarizations, respectively.

A resonance shift of up to 1.5 nm can be obtained when one increases the thickness from 250 to 300 nm ($w=330$ nm, TE polarization), while every additional layer of SiO₂ leads to a decreasing shift in the resonance (see Fig. 5). Devices with a smaller width ($w=330$ nm) experience a larger shift as they have optical modes with weaker confinements, and thus are more susceptible to modifications of their refractive index environment.

Fine-tuning using a laser. While the tuning with SiO₂ cladding can strongly shift the cavity resonance, the tuning is not very accurate, i.e. it is difficult to exactly match the measured wavelength with the desired theoretically predicted value. We suggest that our method could be complementary to other methods for fine-tuning: depositing the SiO₂ cladding brings the resonance close to the desired wavelength, and precise tuning can then be achieved by other methods. This two-step approach can be useful when tuning requires significant power consumption and/or heat dissipation. One particular scenario is when cavities with nanoparticles containing SPEs are used at cryogenic temperatures. The heat produced by the chip can degrade the properties of SPEs, for example, by causing the drift or broadening of the emission line.

We demonstrate this two-step tuning approach by first depositing a 300 nm cladding, then heating the cavity with the 532 nm pump laser in the confocal microscopy setup. By adjusting the laser power, we can precisely tune the resonant frequency line of the cavity within the range of 12 pm, see Fig. 6. We assume that some inaccuracy in the measurements may occur due to the instability of the tunable laser used to measure resonance line profiles, which has limited mode-hop-free tuning range. We verified that the resonance shifts can be attributed to the laser heating by blocking the laser heating beam, which immediately resulted in the return of resonant line to the initial position. We note that the shifts are due to absorption of the heating laser by the SiO₂ cladding, as we do not observe any shifts with an exposed Si₃N₄ cavities, i.e. before SiO₂ cladding. We note that even though both SiO₂ and Si₃N₄ have approximately the same thermo-optic coefficient, SiO₂ has an order of magnitude smaller thermal conductivity, which we assume would help to localize the heat at the vicinity of the cavity³⁷. To further verify that the laser-induced heating is localised, we moved the laser spot 2 μ m away from the cavity. We observed that the cavity resonance line returns to the initial position (without laser heating). Thus we demonstrate that the cavity can be fine-tuned using the combination of cladding deposition and localized laser heating.

We note that we cannot directly determine the heating efficiency; using a simplified assumption that all the laser power is transformed into heat without any losses, we obtain a fine-tuning rate of ~ 0.36 nm/W, i.e. ~ 0.1 FSR

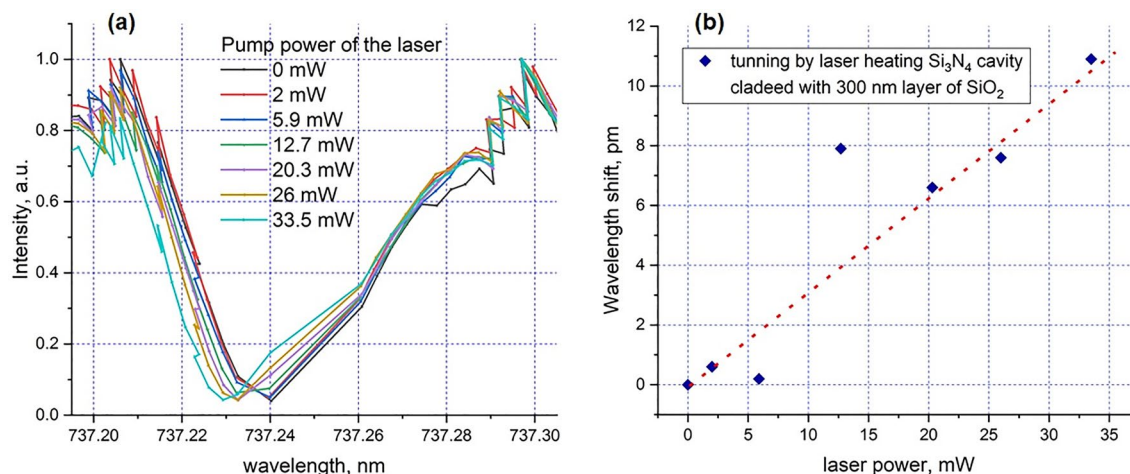


Figure 6. Experimental tuning of the resonance wavelength for Si_3N_4 ring cavity clad with 300 nm of SiO_2 by local heating with 532 nm laser. **(a)** Spectral profiles of the cavity resonances for different laser powers; **(b)** the dependence of reversible shift of the central resonance wavelength on applied pump powers of heating 532 nm laser. The red dotted line is a fit indicating the linear dependence of the refractive index (tuning) on temperature.

per W. Although this is an order of magnitude lower than for cavities with integrated heaters^{26,32}, it is sufficient for cavity fine-tuning, and is achievable without the additional fabrication complexity of integrated heaters. However, in practice, SiO_2 is almost transparent at 532 nm wavelength. To increase the heating efficiency, and hence the tuning rate, we could use UV lasers with a wavelength shorter than 350 nm, where the SiO_2 absorption is much stronger.

Integration of the nanoparticles. Integration of nanoparticles hosting SPEs with photonic platforms is one of the main targets for the successful realization of quantum photonics. We demonstrate that depositing a 500 nm SiO_2 cladding does not significantly affect the positioning of nanodiamonds deposited by spin-coating on top of the ring cavities. By comparing Scanning Electron Microscope (SEM) images taken before and after cladding, we find that the position of nanodiamonds does not change within the resolution of the SEM, see Fig. 7a,b. We also verified that the SiV emission from the nanodiamonds do not undergo significant changes in brightness or the spectral properties, Fig. 7c,d. This shows that our tuning method is suitable for photonic cavities with integrated nanoparticles.

Conclusions

We demonstrate a technique for broadband tuning of Si_3N_4 microring cavities. The method is based on the deposition of SiO_2 nanolayers onto the cavities, combined with localized laser heating. Experimental results show good agreement with the theoretical predictions.

The ability to tune the cavity resonance without significant heat dissipation can be important for quantum photonic applications that operate at cryogenic temperatures. In contrast to the application of photochromic or polyelectrolyte films, we do not observe the degradation of the Q-factor. Furthermore, we verify that nanoparticles placed on the cavity are not displaced by the deposition of the cladding, and that their spectral properties do not change.

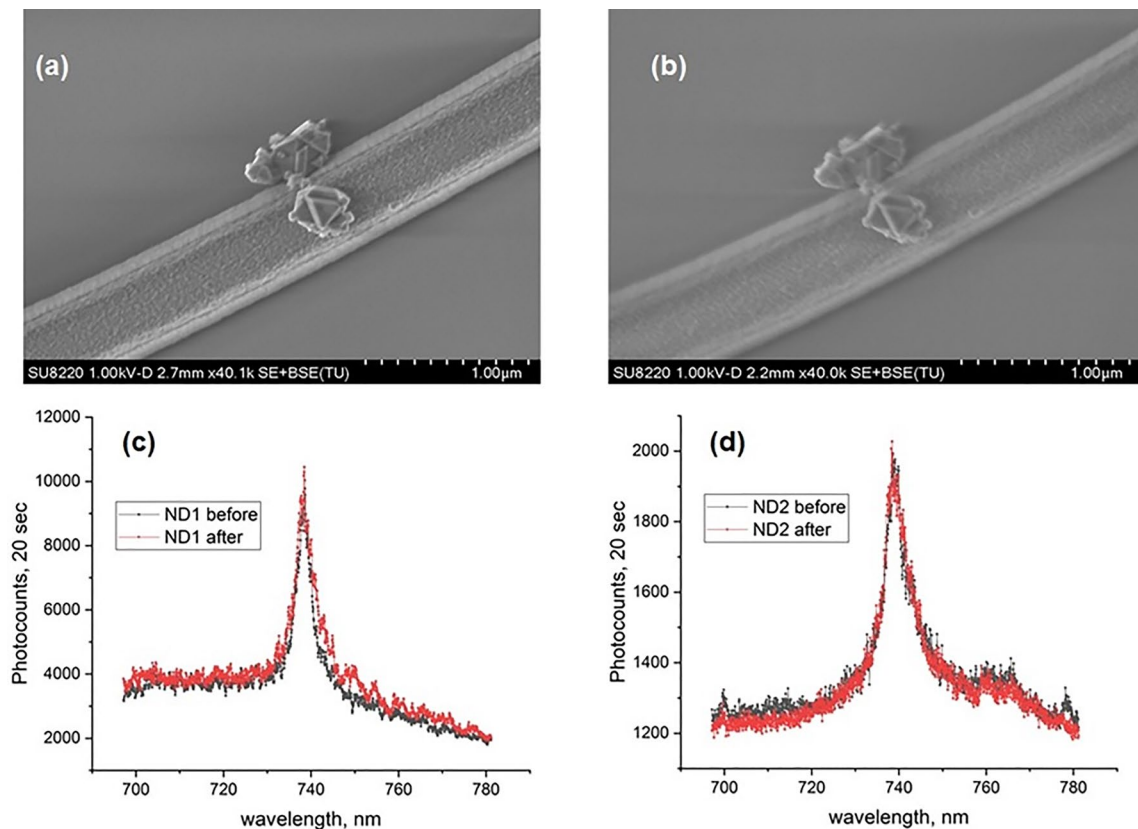


Figure 7. Nanodiamonds before and after SiO₂ deposition of 500 nm thickness. Position of nanodiamonds placed on top of Si₃N₄ ring cavity studied under SEM before (a) and after (b) deposition by spin-coating. Spectral properties of two different nanodiamonds (c and d) before (black) and after (red) SiO₂ deposition obtained in the measurements with confocal microscope setup.

Our technique can be helpful for small-volume, high Purcell-factor cavities with large FSR, where cavity tuning of up to several nanometers can be required. This will be a valuable addition to the toolkit for developing integrated quantum photonic devices.

Data availability

Data may be obtained from the authors upon reasonable request.

Received: 28 June 2022; Accepted: 26 August 2022

Published online: 05 September 2022

References

1. Reed, G. T. Device physics: The optical age of silicon. *Nature* **427**, 595–596 (2004).
2. Jalali, B. Teaching silicon new tricks. *Nat. Photonics* **1**, 193–195 (2007).
3. O'Brien, J. L. Optical quantum computing. *Science* **318**, 1567–1570 (2007).
4. O'Brien, J. L., Furusawa, A. & Vučković, J. Photonic quantum technologies. *Nat. Photonics* **3**, 687–695 (2009).
5. Kimble, H. J. The quantum internet. *Nature* **453**, 1023–1030 (2008).
6. Wang, J. *et al.* Multidimensional quantum entanglement with large-scale integrated optics. *Science* **360**, 285–291 (2018).
7. Qiang, X. *et al.* Large-scale silicon quantum photonics implementing arbitrary two-qubit processing. *Nat. Photonics* **12**, 534–539 (2018).
8. Lee, J. *et al.* Integrated single photon emitters. *AVS Quantum Sci.* **2**, 031701 (2020).
9. Kim, J.-H., Aghaieimobdi, S., Carolan, J., Englund, D. & Waks, E. Hybrid integration methods for on-chip quantum photonics. *Optica* **7**, 291–308 (2020).
10. Elshaari, A. W., Pernice, W., Srinivasan, K., Benson, O. & Zwiller, V. Hybrid integrated quantum photonic circuits. *Nat. Photonics* **14**, 285–298 (2020).
11. Yanikgonul, S. *et al.* Integrated avalanche photodetectors for visible light. *Nat. Commun.* **12**, 1834 (2021).
12. Alagappan, G., Krivitsky, L. A. & Png, C. E. Diamond in a nanopocket: A new route to a strong Purcell effect. *ACS Omega* **3**, 4733–4742 (2018).
13. Hoang, T. B. *et al.* Widely tunable, efficient on-chip single photon sources at telecommunication wavelengths. *Opt. Express* **20**, 21758–21765 (2012).
14. Schwarz, S. *et al.* Electrically pumped single-defect light emitters in WSe₂. *2D Mater.* **3**, 025038 (2016).
15. Mendelson, N. *et al.* Engineering and tuning of quantum emitters in few-layer hexagonal boron nitride. *ACS Nano* **13**, 3132–3140 (2019).
16. Piegdon, K. A. *et al.* All-optical tunability of microdisk lasers via photo-addressable polyelectrolyte functionalization. *Opt. Express* **20**, 6060–6067 (2012).

17. Faraon, A. *et al.* Local tuning of photonic crystal cavities using chalcogenide glasses. *Appl. Phys. Lett.* **92**, 043123 (2008).
18. Shainline, J. M., Fernandes, G., Liu, Z. & Xu, J. Broad tuning of whispering-gallery modes in silicon microdisks. *Opt. Express* **18**, 14345–14352 (2010).
19. Shen, Y., Divliansky, I. B., Basov, D. N. & Mookherjee, S. Electric-field-driven nano-oxidation trimming of silicon microrings and interferometers. *Opt. Lett.* **36**, 2668–2670 (2011).
20. von Klitzing, W., Long, R., Ilchenko, V. S., Hare, J. & Lefèvre-Seguin, V. Frequency tuning of the whispering-gallery modes of silica microspheres for cavity quantum electrodynamics and spectroscopy. *Opt. Lett.* **26**, 166–168 (2001).
21. Niu, N. *et al.* A full free spectral range tuning of p-i-n doped gallium nitride microdisk cavity. *Appl. Phys. Lett.* **101**, 161105 (2012).
22. Hosseini, N. *et al.* Stress-optic modulator in TriPLeX platform using a piezoelectric lead zirconate titanate (PZT) thin film. *Opt. Express* **23**, 14018–14026 (2015).
23. Zhang, M. *et al.* Synchronization of micromechanical oscillators using light. *Phys. Rev. Lett.* **109**, 233906 (2012).
24. Ding, L. *et al.* Wavelength-sized GaAs optomechanical resonators with gigahertz frequency. *Appl. Phys. Lett.* **98**, 113108 (2011).
25. Dong, P. *et al.* Thermally tunable silicon racetrack resonators with ultralow tuning power. *Opt. Express* **18**, 20298–20304 (2010).
26. Lee, B. S. *et al.* On-chip thermo-optic tuning of suspended microresonators. *Opt. Express* **25**, 12109–12120 (2017).
27. Atabaki, A. H., Eftekhari, A. A., Askari, M. & Adibi, A. Accurate post-fabrication trimming of ultracompact resonators on silicon. *Opt. Express* **21**, 14139–14145 (2013).
28. Moss, D. J., Morandotti, R., Gaeta, A. L. & Lipson, M. New CMOS-compatible platforms based on silicon nitride and Hydex for nonlinear optics. *Nat. Photonics* **7**, 1749–1755 (2013).
29. Bauters, J. F. *et al.* Ultra-low-loss high-aspect-ratio Si₃N₄ waveguides. *Opt. Express* **19**, 3163–3174 (2011).
30. Li, Q. *et al.* Vertical integration of high-Q silicon nitride microresonators into silicon-on-insulator platform. *Opt. Express* **21**, 18236–18248 (2013).
31. Gondarenko, A., Levy, J. S. & Lipson, M. High confinement micron-scale silicon nitride high Q ring resonator. *Opt. Express* **17**, 11366–11370 (2009).
32. Elshaari, A. W., Zadeh, I. E., Jöns, K. D. & Zwiller, V. Thermo-optic characterization of silicon nitride resonators for cryogenic photonic circuits. *IEEE Photonics J.* **8**, 2701009 (2016).
33. Fallahkhair, A. B., Li, K. S. & Murphy, T. E. Vector finite difference modesolver for anisotropic dielectric waveguides. *J. Lightwave Technol.* **26**, 1423–1431 (2008).
34. Bogaerts, W. *et al.* Silicon microring resonators. *Laser Photonics Rev.* **6**, 47–73 (2012).
35. Alagappan, G. & Png, C. E. Deep learning models for effective refractive indices in silicon nitride waveguides. *J. Opt.* **21**, 035801 (2019).
36. Choi, S. *et al.* Varying temperature and silicon content in nanodiamond growth: Effects on silicon-vacancy centres. *Sci. Rep.* **8**, 3792 (2018).
37. COMSOL material library.

Acknowledgements

We thank Valery A. Davydov from L.F. Vereshchagin Institute for High Pressure Physics RAS and Viatcheslav N. Agafonov from Université F. Rabelais for the provided nanodiamonds.

Author contributions

D.A.K., G.A. and L.A.K. jointly conceived the idea of the experiment. G.A. and C.E.P. designed the optical devices. T.H. and N.L. fabricated the samples. D.A.K. and V.L. built the chip characterization setup and conducted optical measurements. G.A. and D.A.K. analysed the experimental data. D.A.K. wrote the first draft of the manuscript with the contributions of all co-authors. D.A.K., G.A. and L.A.K. coordinated the project.

Funding

We acknowledge the funding support from the Agency for Science, Technology and Research, Singapore (#21709) and the National Research Foundation, Singapore (Grant No. NRF-CRP14-2014-04).

Competing interests

The authors declare no competing interests.

Additional information

Supplementary Information The online version contains supplementary material available at <https://doi.org/10.1038/s41598-022-19255-9>.

Correspondence and requests for materials should be addressed to D.A.K.

Reprints and permissions information is available at www.nature.com/reprints.

Publisher's note Springer Nature remains neutral with regard to jurisdictional claims in published maps and institutional affiliations.



Open Access This article is licensed under a Creative Commons Attribution 4.0 International License, which permits use, sharing, adaptation, distribution and reproduction in any medium or format, as long as you give appropriate credit to the original author(s) and the source, provide a link to the Creative Commons licence, and indicate if changes were made. The images or other third party material in this article are included in the article's Creative Commons licence, unless indicated otherwise in a credit line to the material. If material is not included in the article's Creative Commons licence and your intended use is not permitted by statutory regulation or exceeds the permitted use, you will need to obtain permission directly from the copyright holder. To view a copy of this licence, visit <http://creativecommons.org/licenses/by/4.0/>.

© The Author(s) 2022